

The Formation of the Hubble Sequence of Disk Galaxies: The Effects of Early Viscous Evolution

Bing Zhang and Rosemary F.G. Wyse ^{*}

Department of Physics and Astronomy, Johns Hopkins University, 3400 N.Charles Street, Baltimore, MD 21218, USA

25 October 2018

ABSTRACT

We investigate a model of disk galaxies whereby viscous evolution of the gaseous disk drives material inwards to form a proto-bulge. We start from the standard picture of disk formation through the settling of gas into a dark halo potential well, with the disk initially coming into centrifugal equilibrium with detailed conservation of angular momentum. We derive generic analytic solutions for the disk-halo system after adiabatic compression of the dark halo, with free choice of the input virialized dark halo density profile and of the specific angular momentum distribution. We derive limits on the final density profile of the halo in the central regions. Subsequent viscous evolution of the disk is modelled by a variation of the specific angular momentum distribution of the disk, providing analytic solutions to the final disk structure. The assumption that the viscous evolution timescale and star formation timescale are similar leads to predictions of the properties of the stellar components. Focusing on small ‘exponential’ bulges, ones that may be formed through a disk instability, we investigate the relationship between the assumed initial conditions, such as halo ‘formation’, or assembly, redshift z_f , spin parameter λ , baryonic fraction F , and final disk properties such as global star formation timescale, gas fraction, and bulge-to-disk ratio. We find that the present properties of disks, such as the scale length, are compatible with a higher initial formation redshift if the re-distribution by viscous evolution is included than if it is ignored. We also quantify the dependence of final disk properties on the ratio F/λ , thus including the possibility that the baryonic fraction varies from galaxy to galaxy, as perhaps may be inferred from the observations.

Key words: galaxies: formation — galaxies: structure — galaxies: spiral — cosmology: theory — dark matter

1 INTRODUCTION

The current picture of disk galaxy formation and evolution has as its basis the dissipative infall of baryons within a dominant dark halo potential well (White & Rees 1978). The collapse and spin-up of the baryons, with angular momentum conservation, can provide an explanation for many of the observed properties of disks, with the standard initial conditions of baryonic mass fraction $F \sim 0.1$ and dark halo angular momentum parameter $\lambda \sim 0.07$ (Fall & Efstathiou 1980; Gunn 1982; Jones & Wyse 1983; Dalcanton, Spergel & Summers 1997; Hernandez & Gilmore 1998; Mo, Mao & White 1998; van den Bosch 1998). Galaxies such as

the Milky Way which have an old stellar population in the disk, must, within the context of a hierarchical-clustering scenario, evolve through only quiescent merging/accretion, so as to avoid excessive heating and disruption of the disk (Ostriker 1990). Further, the merging processes with significant substructure cause angular momentum transport to the outer regions, which must somehow be suppressed to allow the formation of extended disks as observed (e.g. Zurek, Quinn & Salmon 1988; Silk & Wyse 1993; Navarro & Steinmetz 1997).

Thus here we adopt the simplified picture that disk galaxies form from smooth gaseous collapse to centrifugal equilibrium, within a steady dark halo potential. We discuss where appropriate below how this may be modified to take account of subsequent infall, or earlier star formation. Our

^{*} E-mail: bingz@pha.jhu.edu (BZ); wyse@pha.jhu.edu (RFGW)

model incorporates the adiabatic response of the dark halo to the disk infall, and we provide new, more general, analytic solutions for the density profile, given a wide range of initial density profiles and angular momentum distributions. We provide new insight into the ‘disk-halo’ conspiracy within the context of this model, demonstrating how an imperfect conspiracy is improved by the disk-halo interaction. We explicitly include subsequent viscous evolution of the gas disk to provide the exponential profile of the stellar disk, and develop analytic expressions that illustrate the process. The resulting radial inflow builds up the central regions of the disk and we investigate the properties of ‘bulges’ that may form as a consequence of instabilities of the central disk. We derive new constraints on the characteristic redshift of disk star formation. We obtain a simple relation connecting the initial conditions, such as spin parameter and baryonic mass fraction, to the efficiency of viscous evolution and star formation.

2 THE DISK GALAXY FORMATION MODEL

In this section we shall derive the mass profiles of disk and halo after the collapse of the baryons. We shall follow earlier treatments of disk galaxy formation (e.g. Mo, Mao & White 1998) by assuming that the virialized dark halo, mixed with baryonic gas, is ‘formed’ – or at least assembled – at redshift z_f . This virialized halo has a limiting radius r_{200} within which the mean density is $200\rho_{crit}(z_f)$, and contains a baryonic mass fraction F . Then

$$r_{200} = \frac{V_{200}}{10H(z_f)}; \quad M_{tot} = \frac{V_{200}^2 r_{200}}{G} = \frac{V_{200}^3}{10GH(z_f)}, \quad (1)$$

where $H(z_f)$ is the value of the Hubble parameter at redshift z_f , $M_{tot}(z_f)$ is the total mass within virialized radius r_{200} , and V_{200} is the circular velocity at r_{200} .

The baryonic gas cools and settles into a disk, causing the dark halo to contract adiabatically (Blumenthal *et al.* 1986). The specific angular momentum distribution of the gas is assumed to be conserved during these stages. We shall include below the subsequent re-arrangement of the disk due to angular momentum transport. This we investigate by variation of the disk angular momentum distribution function, choosing an appropriate analytic functional form. Let $m_d(r)$ and $m_h(r)$ respectively denote the fraction of the total baryonic mass, and total dark mass, that is contained within radius r , and denote the baryonic mass angular momentum distribution function by

$$m_d(< j) = f(j/j_{max}), \quad (2)$$

where j_{max} is the maximum specific angular momentum of the disk.

We will be requiring that the functional form, $f(j/j_{max})$, vary as the disk evolves, and it is convenient to introduce the notation $\ell \equiv j/j_{max}$ and define

$$c_f \equiv 1 - \int_0^1 f(\ell) d\ell, \quad (3)$$

which represents the area above the angular momentum distribution function curve $f(\ell)$ for $0 \leq \ell \leq 1$. We will mimic the effects of viscous evolution by decreasing the value of c_f in our evolving disk models in section 4 below.

In terms of this parameter the total disk angular momentum is:

$$\begin{aligned} J_d &= FJ_{tot} = M_d \int_0^{j_{max}} j \frac{dm_d}{dj} dj \\ &= M_d j_{max} \left(1 - \int_0^1 f(\ell) d\ell \right) = FM_{tot} j_{max} c_f, \end{aligned} \quad (4)$$

with $M_d = FM_{tot}$. Thus $j_{max}c_f$ is the average specific angular momentum of the disk material.

The specific angular momentum of the disk material is assumed to follow that of the dark halo, but in general will not be a simple analytic function (e.g. Quinn & Binney 1992). For illustration, we adopt an analytic monotonic increasing function $f(b, \ell)$ containing a free parameter b , with $0 \leq b \leq 1$. We require the initial angular momentum distribution to be scale free, representing the angular momentum distribution of the virialized halo, and will adopt $f(b=0, \ell) = \ell^n$. We shall vary the value of the parameter b to mimic the effects of viscous evolution on the angular momentum distribution.

The total energy is:

$$E_{tot} = -\frac{\epsilon_0 GM_{tot}^2}{2r_{200}} = -\frac{\epsilon_0 M_{tot} V_{200}^2}{2}, \quad (5)$$

where ϵ_0 is a constant of order unity, depending on the dark halo density profile, and since it is constant for any specific halo model, we can take $\epsilon_0 = 1$ without loss of generality. The spin parameter λ is by definition

$$\lambda \equiv J_{tot} |E_{tot}|^{1/2} G^{-1} M_{tot}^{-5/2}. \quad (6)$$

Thus the mean specific angular momentum of the disk material may be expressed as

$$c_f j_{max} = \sqrt{2} \lambda V_{200} r_{200}. \quad (7)$$

Assuming spherical symmetry, the rotationally-supported disk has mass profile given by

$$m_d = f(j/j_{max}) = f\left(\frac{\sqrt{GM_{tot}(m_d)} r(m_d)}{j_{max}}\right) = f(\ell), \quad (8)$$

while the initial virialized halo mass profile is

$$g(R_{ini}) = m_h(R_{ini}) = M_{ini}(R_{ini})/M_{tot}, \quad (9)$$

with $R \equiv r/r_{200}$.

2.1 Constraints on the Final Dark Halo Profile and Mass Angular Momentum Distribution Function

The above equations describe the disk and halo just upon the settling of the gas disk to the mid-plane, prior to the subsequent adiabatic compression of the halo. A self-consistent calculation of the modified disk and halo density profiles may be made by consideration of the adiabatic invariance of

the angular action, $I_\theta \equiv \int v_\theta \cdot r d\theta = \sqrt{GM_{tot}(r)}r$, together with the assumption of no shell crossing (cf. Blumenthal *et al.* 1986).

Suppose a dark matter particle initially at r_{ini} finally settles at $r(m_d)$, the radius within which the dark halo mass fraction is m_h . Then under adiabatic invariance the disk mass profile, m_d , and the halo mass profile, m_h , are related by:

$$GM_{tot}(m_d)r(m_d) = GM_{tot}(m_h)r(m_h) \quad (10)$$

$$= GM_{ini}(m_h)r_{ini}(m_h) \quad (11)$$

$$= GM_{tot}m_h r_{200}g^{-1}(m_h), \quad (12)$$

where $g^{-1}(m_h)$ is the inverse function of $g(R)$, the initial virialized halo mass profile.

Further manipulation of these relations is simplified by introduction of the parameter ξ , given by

$$\xi \equiv \frac{\sqrt{GM_{tot}r_{200}}}{j_{max}} = \frac{c_f}{\sqrt{2}\lambda}. \quad (13)$$

Generally ξ is a quantity that is closely related to the overall disk collapse factor.

From equations (8) and (12), we have

$$m_d = f(\ell), \quad (14)$$

$$\ell = \xi (m_h g^{-1}(m_h))^{1/2}, \quad (15)$$

where ℓ is the normalized specific angular momentum. Again, $0 \leq \ell \leq 1$, and $\ell = 1$ corresponds to the maximum specific angular momentum of the disk, which occurs at the edge of the disk, equivalently at the disk cutoff radius. The fraction of the dark matter contained within the disk thus has a maximum value, m_{hc} , given by $\ell = 1$ in the above equation, and for radii with $m_h \geq m_{hc}$, $m_d = 1$.

To illustrate the physical meaning of these parameters, consider the rigid singular isothermal halo, for which $g(m_{hc}) = m_{hc} = R_c$. Then from equation (15), $R_c = R(\ell = 1) = 1/\xi$ which corresponds to the disk cutoff radius. Thus in this case, remembering that R is the normalized radius, $\xi = 1/R_c$ is the disk collapse factor.

Up to now we know the mass profile of disk and halo after collapse, in terms of the normalized specific angular momentum ℓ , as given in equations (14) and (15), for given forms of the angular momentum distribution function, f , and initial virialized dark halo mass profile, g . Next we shall obtain the relation between ℓ and radius R , to complete the derivation of the mass profiles of disk and halo after collapse.

Returning to a general halo density profile, the total mass contained within the radius corresponding to m_h is

$$M(m_h) = M_{tot}((1-F)m_h + Fm_d). \quad (16)$$

From equations (9) - (12) and (16), we have

$$R = \frac{GM_{ini}(m_h)r_{ini}(m_h)}{GM(m_h)r_{200}} \quad (17)$$

$$= \frac{m_h g^{-1}(m_h)}{(1-F)m_h + Fm_d}. \quad (18)$$

Introducing the radius variable x and coefficient c_0 as

$$x \equiv \xi(1-F)R, \quad (19)$$

$$c_0 \equiv \xi F/(1-F), \quad (20)$$

we may finally derive the functional dependences on ℓ of the disk mass m_d , of the halo mass m_h , and of the radius x :

$$m_d = f(\ell), \quad (21)$$

$$m_h g^{-1}(m_h) = \frac{\ell^2}{\xi^2}, \quad (22)$$

$$x = \frac{\ell^2}{\xi m_h(\ell) + c_0 f(\ell)}. \quad (23)$$

Thus ℓ can be thought of as a normalized radius. As we shall see later, c_0 is a measure of the compactness of the final collapsed disk due to the competition between the spin parameter λ and the baryonic mass fraction F .

These equations (21) - (23) can be used to derive disk and halo properties for a free choice of virialized halo profile $g(R)$ and angular momentum distribution function $f(\ell)$. Within the disk cutoff radius, with $0 \leq \ell \leq 1$, the disk surface density, circular velocity and the disk-to-dark mass ratio as function of radius ℓ or R have the generic forms:

$$\Sigma_d = \frac{10H(z)FV_{200}}{2\pi G} \frac{1}{R} \frac{df}{d\ell} \frac{d\ell}{dR}, \quad (24)$$

$$V_c = \frac{V_{200}\ell}{\xi R}, \quad (25)$$

$$\frac{M_d(\ell)}{M_h(\ell)} = \frac{c_0 f(\ell)}{\xi m_h(\ell)}, \quad (26)$$

where $M_d(\ell) = M_d(\ell = 1)m_d(\ell) = M_d m_d(\ell)$ and $M_h(\ell)$ is defined similarly.

The circular velocity at radii beyond the disk cutoff, but within the halo, is given by:

$$V_c = \frac{V_{200} \sqrt{m_h g^{-1}(m_h)}}{R}, \quad (27)$$

$$R = \frac{m_h g^{-1}(m_h)}{(1-F)m_h + F}. \quad (28)$$

Armed with these relations, one may now look at various initial virialized halo density profiles and angular momentum distributions, and determine the allowed parameter space from observed properties of disk galaxies. It is convenient to adopt power-law approximations for the initial virialized halo mass profile and angular momentum distributions, such that $m_h(\ell) \sim \ell^m$ and $f(\ell) \sim \ell^n$ for small ℓ . Figure 1 shows the location of various fiducial models in the plane of these power law indices m and n ; the value $m = 1$ corresponds to the singular isothermal sphere, the value $m = 4/3$ corresponds to the Hernquist (1990) and to the Navarro, Frenk & White (1997) profiles, while the value $m = 3/2$ corresponds to the non-singular isothermal sphere with a constant-density core. These profiles span the range of dark-halo profiles suggested by theory, and plausibly consistent with observations. The shaded region is the allowed parameter space for these models, constrained by the surface-density profile, rotation curve and disk-to-halo central mass ratio. The line ABC is the maximum angular-momentum index consistent with a disk surface density profile in the central regions that declines with increasing radius, while the line DEF is the minimum angular-momentum index consistent with a finite value of the central circular velocity. The

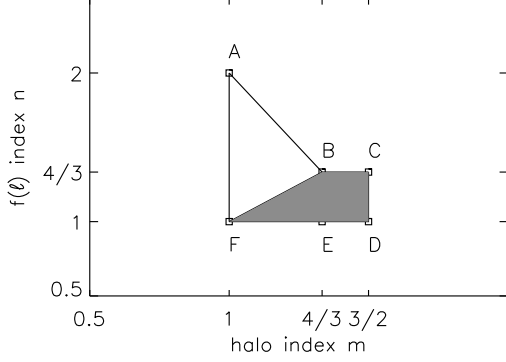


Figure 1. The power-law approximations for the initial virialized halo mass profile and angular momentum distributions are $m_h(\ell) \sim \ell^m$ and $f(\ell) \sim \ell^n$ for small ℓ . The shaded region is the allowed parameter space for these models, constrained by the surface-density profile, rotation curve and disk-to-halo central mass ratio. The line ABC is the maximum angular-momentum index consistent with a disk surface density profile in the central regions that declines with increasing radius, while the line DEF is the minimum angular-momentum index consistent with a finite value of the central circular velocity. The line BF denotes the maximum values of n consistent with a non-zero central disk-to-halo mass ratio. The value $m = 1$ corresponds to the singular isothermal sphere, the value $m = 4/3$ corresponds to the Hernquist (1990) and to the Navarro, Frenk & White (1997) profiles, while the value $m = 3/2$ corresponds to the non-singular isothermal sphere with a constant-density core.

line BF denotes the maximum values of n consistent with a non-zero central disk-to-halo mass ratio.

This power-law approximation has an initial virialized halo density profile at small radius as $\rho_{h,ini}(R) \sim R^{\frac{m}{2-m}-3}$ (seen by solution of (22) for the form of g). Solving equations (21) - (23) above gives the corresponding profile after adiabatic infall. In the central region, where the disk dominates the gravitational potential (i.e. $c_0 f(\ell) \gg \xi m_h(\ell)$), the halo density profile is $\rho_h(R) \sim R^{\frac{m}{2-n}-3}$. Note that in the region where the dark halo dominates the gravitational potential (i.e. $c_0 f(\ell) \ll \xi m_h(\ell)$), the halo density profile is essentially unaffected by the disk, as expected.

For the case $n = m$, the central halo density profile is unaffected since the disk mass density profile and the initial virialized halo density profile have the same dependence on ℓ . The viable models within the shaded region have $n \leq m$, so that the final halo density profile in the central, disk-dominated region should be steeper than its initial virialized profile in this region, not surprisingly. Thus the final halo profile for these models ranges from $\rho_h \sim R^{-0.75}$ to $\rho_h \sim R^{-2}$. It is interesting to note that $\rho_h \sim R^{-0.75}$, the outcome of an initial virialized halo with a constant density core responding to the settling of a disk with angular momentum index $n = 4/3$, corresponds to the de-projected de Vaucouleurs central density profile. Thus provided the virialized halo does not have a declining density profile with decreasing radius, which is unphysical, the final dark halo cannot have a constant density core, at least in the very central region where the disk dominates, but should be cuspy.

2.2 The Singular Isothermal Sphere

The singular isothermal sphere provides a virialized halo density profile that is the most tractable analytically, and we can obtain some important scaling relations without having to specify the angular momentum distribution $f(\ell)$; aspects of the analysis of this profile should hold in general, and provide insight.

The final disk and halo mass profiles are given by solution of:

$$x = \frac{\ell}{1 + c_0 \frac{f(\ell)}{\ell}}, \quad (29)$$

$$m_h = \ell/\xi, \quad (30)$$

$$m_d = f(\ell), \quad (31)$$

where $0 \leq \ell \leq 1$ and c_0 and ξ , the parameters describing the compactness of the collapsed disk and its collapse factor, are defined above in equations (20) and (13).

The collapse factor, defined as the ratio of the pre-collapse radius r_{200} to the cutoff disk radius r_c at $\ell = 1$ (to be distinguished from the final disk scale length) is

$$\frac{r_{200}}{r_c} = \xi(1 - F)(1 + c_0) = \frac{c_f}{\sqrt{2}\lambda} \left(1 - F + \frac{c_f F}{\sqrt{2}\lambda}\right), \quad (32)$$

where c_f , defined in equation (3), is a measure of the shape of the angular momentum distribution, and small values of c_f mean steeply-rising angular momentum distributions.

Typical angular momentum distributions for disks are shown in Figure 2 (a,b) and discussed below. Here one should just note that a value $c_f \sim 0.5$ is reasonable. With this, and $\lambda = 0.06$ and $F = 0.1$, we obtain $\xi = 5.9$ and $c_0 = 0.66$. The collapse factor as defined here is then about a factor of 9. For fixed angular momentum distribution c_f , the collapse factor depends not only on $1/\lambda$ but also on compactness $c_0 \propto F/\lambda$. This is consistent with the results of previous studies of the collapse factor in two extreme cases (Jones & Wyse 1983; Peebles 1993): if the final disk is so self-gravitating that the value of F/λ corresponds to $c_0 \gg 1$, then the collapse factor is $\propto F/\lambda^2$; on the other hand if the final disk is sufficiently far from self-gravitating, with small F/λ and $c_0 \ll 1$, the collapse factor is $\propto 1/\lambda$. The above collapse factor relationship is valid over the entire range of values for the parameters λ and F (and is the most general relation derived to date).

It should be noted that varying the normalized angular momentum distribution by varying c_f changes the derived collapse factor; this is investigated further below.

Comparison between the sizes of observed disks and those predicted from such collapse calculations provides a constraint on the redshift at which the collapse happened (e.g. Mo, Mao & White 1998). Our disk cutoff radius for non-trivial $f(\ell)$ may be expressed in terms of the initial conditions as :

$$r_c = \frac{\sqrt{2}\lambda V_{200}}{10H(z_f)c_f(1 - F + \frac{c_f F}{\sqrt{2}\lambda})}, \quad (33)$$

where z_f is the ‘formation’ or assembly redshift, at which the halo is identified to have given mass and circular velocity, with no mass infall after this epoch. One can see from

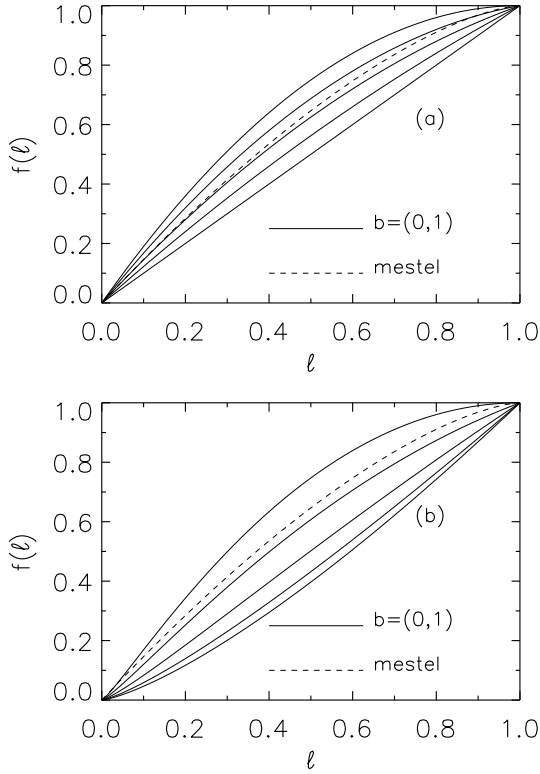


Figure 2. The angular momentum distribution function for the Mestel profile, $f(\ell) = 1 - (1 - \ell)^{3/2}$, is shown by the dashed line. (a) The angular momentum distribution function is $f(b, \ell) = (1 + b)\ell - b\ell^2$ for models on line FED in Figure 1. The different curves correspond to $b = 0, 1/4, 1/2, 3/4, 1$. (b) The angular momentum distribution function is $f(b, \ell) = (1 + 10b)\ell^{4/3} - 10b\ell^{22/15}$ for models on line BC in Figure 1. The different curves correspond to $b = 0, 0.1, 0.3, 0.6, 1$.

this relation that both λ and F/λ are equally important; previous determinations considered the baryonic mass fraction fixed (Dalcanton, Spergel & Summers 1997; Mo, Mao & White 1998).

The explicit inclusion of the parameter c_f allows us to take account of disk evolution, as gas is transformed to stars. Adopting a disk cutoff radius at three disk scale-lengths (e.g. van der Kruit 1987), and choosing specific values of the present-day stellar disk scale-length $r_d = 3.5\text{kpc}$, $\lambda = 0.06$, $V_{200} = 200\text{ km s}^{-1}$ and an Einstein-de-Sitter Universe with Hubble constant $0.5 < h < 1$, the above relation gives the formation redshift $1.6 < z_f < 3.1$ for $F = 0.05$ and $c_f = 1/3$; $1.4 < z_f < 2.8$ for $F = 0.1$ and $c_f = 1/3$; $0.9 < z_f < 2.0$ for $F = 0.05$ and $c_f = 1/2$; $0.7 < z_f < 1.7$ for $F = 0.1$ and $c_f = 1/2$.

Consistent with previous calculations, for fixed formation redshift smaller values of λ can lead to smaller disk size; we have here explicitly demonstrated that larger F/λ can also lead to this result. Lower values of c_f also lead to higher redshift of formation. Thus for no viscous evolution i.e. there is no angular momentum redistribution during the evolution of the galactic disk and c_f has a time-independent value, the

formation redshift z_f determined by assuming fixed initial λ and F and fixed disk size r_c is smaller than would be determined if c_f could be decreased (to mimic say viscous evolution). Lower values of c_f for given total angular momentum content imply a larger disk scale-length; the effect of viscous evolution is to re-arrange the disk material so as to increase the disk scale-length. Typical values of viscosity parameters lead to a factor of 1.5 increase in disk scale-length in a Hubble time. As we demonstrate below, a smaller value for c_f corresponds to larger bulge-to-disk ratio. This result is consistent with the results of Mo, Mao & White (1998): halo and disk formation redshift can be pushed to higher value when a bulge is included. These trends are general, and not tied to the specific model of the halo density profile.

One should bear in mind that the old stars in the local thin disk of the Milky Way have ages of at least 10 Gyr, and may be as old as the oldest stars in the Galaxy (Edvardsson *et al.* 1993); the age distribution of stars at other locations of the Galactic disk is very poorly-determined, but it is clear that a non-trivial component of the thin disk was in place at early times (at redshift $z > 2$ for the cosmologies considered above). A common assumption in previous work is that the mass angular momentum distribution of the disk is that of a solid-body, rotating uniform density sphere, $f(\ell) = 1 - (1 - \ell)^{3/2}$ (Mestel 1963). For this distribution, $c_f = 0.4$, and one derives a low redshift of formation for a galaxy like the Milky Way (Mo, Mao & White 1998), which has difficulties with the observations.

2.2.1 The Singular Isothermal Halo with Simple $f(\ell)$

Analytic solutions to equations (29) - (31) can be obtained by assuming a simple monotonic increasing function $f(b, \ell)$ containing one parameter b with $0 \leq b \leq 1$. In order to avoid the situation where one obtains a trivial collapse factor due to a very small amount of disk material at very large radius, we restrict the shape of the mass angular momentum distribution function $f(\ell)$ to avoid too shallow an asymptotic slope as f approaching 1 when ℓ increases (see Figure 2). From Figure 1, the singular isothermal halo at point F requires $f(\ell) \sim \ell$ for $\ell \ll 1$. A simple form consistent with this is $f(\ell) = (1 + b)\ell - b\ell^2$ with $0 \leq \ell \leq 1$ and $0 \leq b \leq 1$. The angular momentum parameter $c_f = (3 - b)/6$. Figure 2a shows this angular momentum distribution function with different values of the parameter b , compared with the mass angular momentum distribution of a solid-body, rotating uniform density sphere, $f(\ell) = 1 - (1 - \ell)^{3/2}$ (Mestel 1963). The normalized total angular momentum c_f corresponds to the area above each curve.

Within the disk, where $0 \leq \ell \leq 1$, the galactic disk surface density, circular velocity and the disk-to-dark mass ratio as a function of radius are:

$$\Sigma_d(\ell) = \frac{10V_{200}H(z)F(1 - F)^2\xi^2}{\pi G} \times \frac{(1 + b - 2b\ell)(1 + c_0 + c_0b - c_0b\ell)^3}{2\ell(1 + c_0 + c_0b)}, \quad (34)$$

$$V_c(\ell) = V_{200}(1 - F)[1 + c_0(1 + b - b\ell)], \quad (35)$$

$$\frac{M_d(\ell)}{M_h(\ell)} = \frac{(1+b-b\ell)(3-b)F}{6\sqrt{2}\lambda(1-F)}, \quad (36)$$

where

$$\ell = \frac{[1+c_0(1+b)]\xi(1-F)R}{1+bc_0\xi(1-F)R}. \quad (37)$$

From equation (27)-(28), the circular velocity at radii beyond the disk cutoff, but within the halo, is:

$$V_c(R) = \frac{V_{200}(1-F)}{2} \left[1 + \sqrt{1 + \frac{4F}{(1-F)^2 R}} \right]. \quad (38)$$

These results are plotted in Figure 3 (a,b,c) for $\lambda = 0.06$, $F = 0.1$, $0 \leq \ell \leq 1$. The different curves correspond to $b = 0, 1/4, 1/2, 3/4, 1$. Larger values of b yield larger disk cut-off radii; note that the circular velocities for points beyond the cut-off radius of a given model may be obtained by forming the envelope of the values for the cut-off radius for larger values of b . Varying the value of the parameter b changes the angular momentum distribution function similar to the effects of viscous evolution; the ratio of disk mass to dark halo mass increases at small radius with increasing b , which can be interpreted as due to radial inflow of disk material.

2.2.2 Halo Density Profile and Angular Momentum Combinations

For initial virialized halo profiles other than the singular isothermal sphere, the collapse factor has a more general form:

$$\frac{r_{200}}{r_c} = \xi(1-F)(\xi m_{hc} + c_0), \quad (39)$$

where m_{hc} is the solution of $1 = \xi^2 m_{hc} g^{-1}(m_{hc})$ and is the mass fraction of the dark halo that is contained within the cut-off radius of the disk. The trend of the dependence of the collapse factor on the values of λ and F remains the same as found above for the singular isothermal halo.

The range of viable models represented by the shaded region in Figure 1 can be investigated by the appropriate virialized halo profile $g(R)$ and angular momentum distribution function $f(b, \ell)$ corresponding to the points E, B, D and C. The distribution of surface density, circular velocity and disk-to-halo mass ratio for these models, varying parameter b , are shown in Figures 4-7, by choosing fixed $\lambda = 0.06$, $F = 0.1$ (and halo core size $c = 4$ if the halo has a core radius).

Model E: The results of a model corresponding to point E in Figure 1 are shown in Figure 4; this has a Hernquist halo profile $g(R) = \frac{(1+c)^2 R^2}{(1+cR)^2}$ and $f(b, \ell) = (1+b)\ell - b\ell^2$. The different curves correspond to $b = 0, 1/4, 1/2, 3/4, 1$.

Model B: The results of a model corresponding to point B in Figure 1 are shown in Figure 5; this has a Hernquist halo profile $g(R) = \frac{(1+c)^2 R^2}{(1+cR)^2}$ and $f(b, \ell) = (1+10b)\ell^{4/3} - 10b\ell^{22/15}$. This $f(b, \ell)$ is shown in Figure 2b. For $\ell \ll 1$, $f(b=0, \ell) \sim \ell^{4/3}$; the 22/15 index in the second term is determined by the requirement that $f(b, \ell)$ should be a monotonic increasing function of ℓ for all values of $0 \leq b \leq 1$. The different curves correspond to $b = 0, 0.1, 0.3, 0.6, 1$.

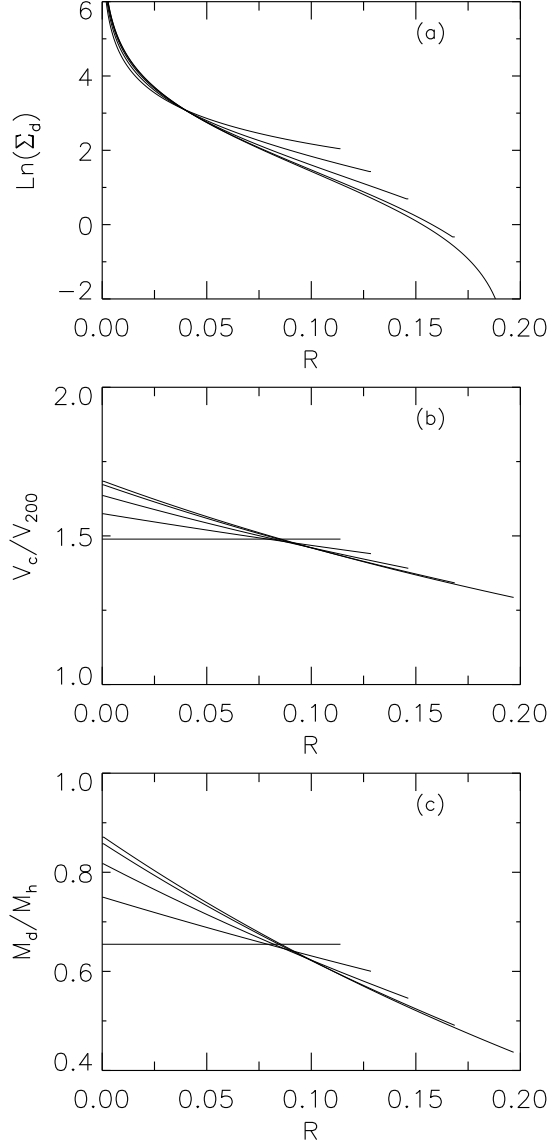


Figure 3. The model corresponding to point F in Figure 1. (a) the surface density, (b) circular velocity and (c) disk-to-halo mass ratio with $\lambda = 0.06$ and $F = 0.1$. The virialized halo is a singular isothermal sphere. The angular momentum distribution function is $f(b, \ell) = (1+b)\ell - b\ell^2$. The different curves correspond to $b = 0, 1/4, 1/2, 3/4, 1$. Larger values of b yield larger disk cut-off radii. The disk-to-halo mass ratio increases slightly when approaching the centre.

Model D: The results of a model corresponding to point D in Figure 1 are shown in Figure 6; this has a non-singular isothermal halo with a constant density core, $g(R) = \frac{cR - \arctan(cR)}{c - \arctan(c)}$, and $f(b, \ell) = (1+b)\ell - b\ell^2$. Again the different curves correspond to $b = 0, 1/4, 1/2, 3/4, 1$.

Model C: The results of a model corresponding to point C in Figure 1 are shown in Figure 7; this has a non-singular isothermal halo with constant density core, $g(R) = \frac{cR - \arctan(cR)}{c - \arctan(c)}$, and $f(b, \ell) = (1+10b)\ell^{4/3} - 10b\ell^{22/15}$. Again the different curves correspond to $b = 0, 0.1, 0.3, 0.6, 1$.

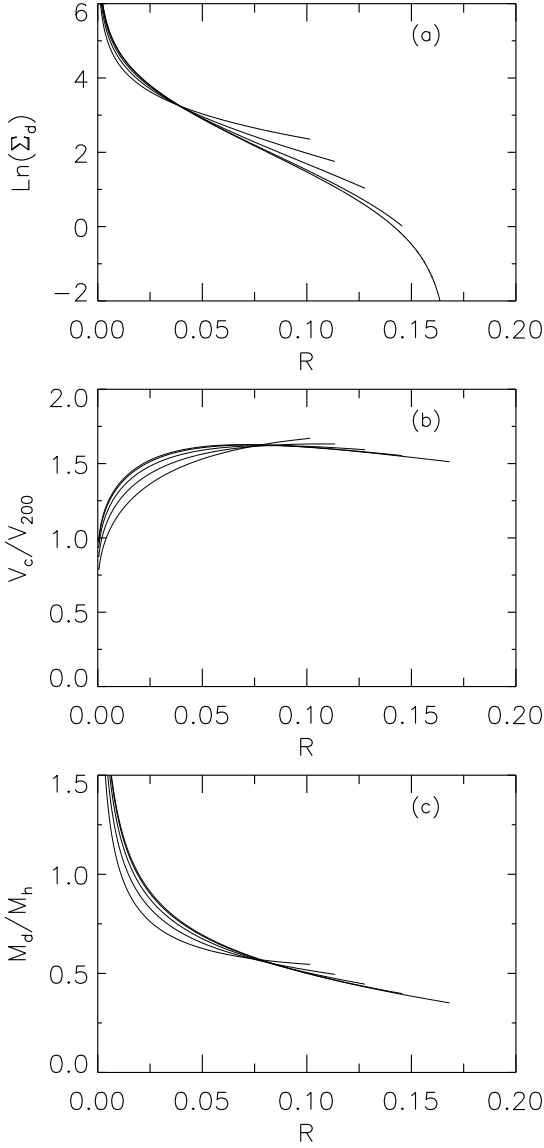


Figure 4. The model corresponding to point E in Figure 1. (a) the surface density, (b) circular velocity and (c) disk-to-halo mass ratio with $\lambda = 0.06$ and $F = 0.1$. The virialized halo is Hernquist halo with core size $c = 4$. The angular momentum distribution function is $f(b, \ell) = (1+b)\ell - b\ell^2$. The different curves correspond to $b = 0, 1/4, 1/2, 3/4, 1$. The disk-to-halo mass ratio increases significantly when approaching the centre.

As can be seen from the figures, the different halo profiles and angular momentum distributions produce disks with a variety of surface density profiles and rotation curves. As in Figure 3b, the circular velocities for points beyond the cut-off radius of a given model may be obtained by forming the envelope of the values for the cut-off radius for larger values of b . Thus if the disk is very compact, from equations (27)-(28) or equation (38), we find that the circular velocity beyond the edge of the disk tends to decrease with radius. The location of the edge of the disk depends on both λ and F (in addition to b). Thus we have shown that rota-

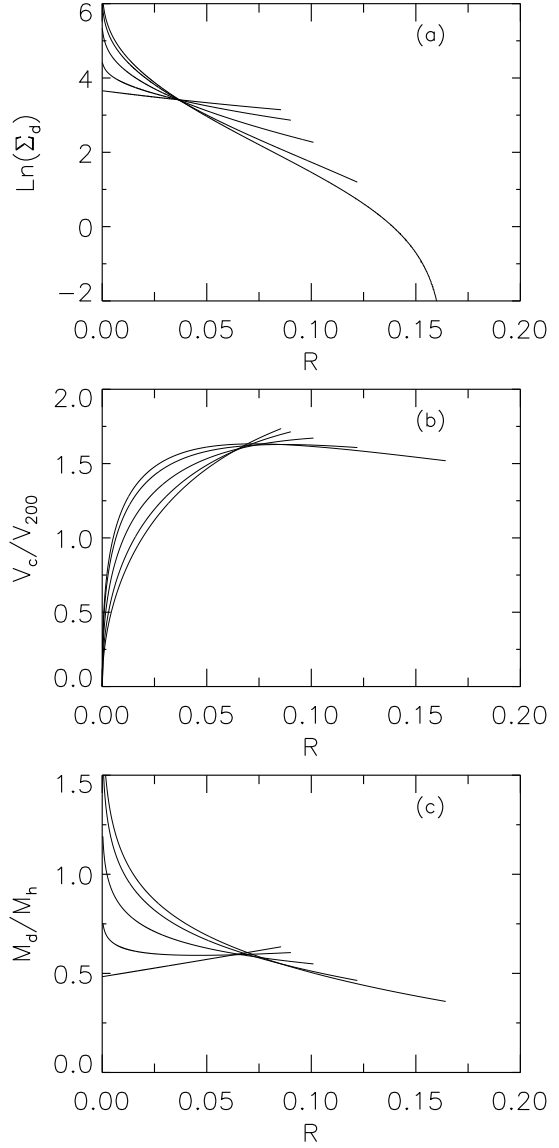


Figure 5. The model corresponding to point B in Figure 1. (a) the surface density, (b) circular velocity and (c) disk-to-halo mass ratio with $\lambda = 0.06$ and $F = 0.1$. The virialized halo is Hernquist halo with core size $c = 4$. The angular momentum distribution function is $f(b, \ell) = (1+10b)\ell^{4/3} - 10b\ell^{22/15}$. The different curves correspond to $b = 0, 0.1, 0.3, 0.6, 1$. The disk-to-halo mass ratio increases but not significantly when approaching the centre.

tion curves should show an imperfect disk-halo ‘conspiracy’ if the disk is too compact or too massive. This is consistent with observations (Casertano & van Gorkom 1991).

Further, these figures demonstrate that with increasing b , the inner rotation curves become flat, and the transition between disk-dominated and halo-dominated sections of the rotation curve becomes more and more smooth with increasing b . As discussed above, and illustrated in Figure 2, a higher value of b corresponds to a flatter specific angular momentum distribution function, and increasing b mimics the effects of viscous evolution in transporting angular mo-

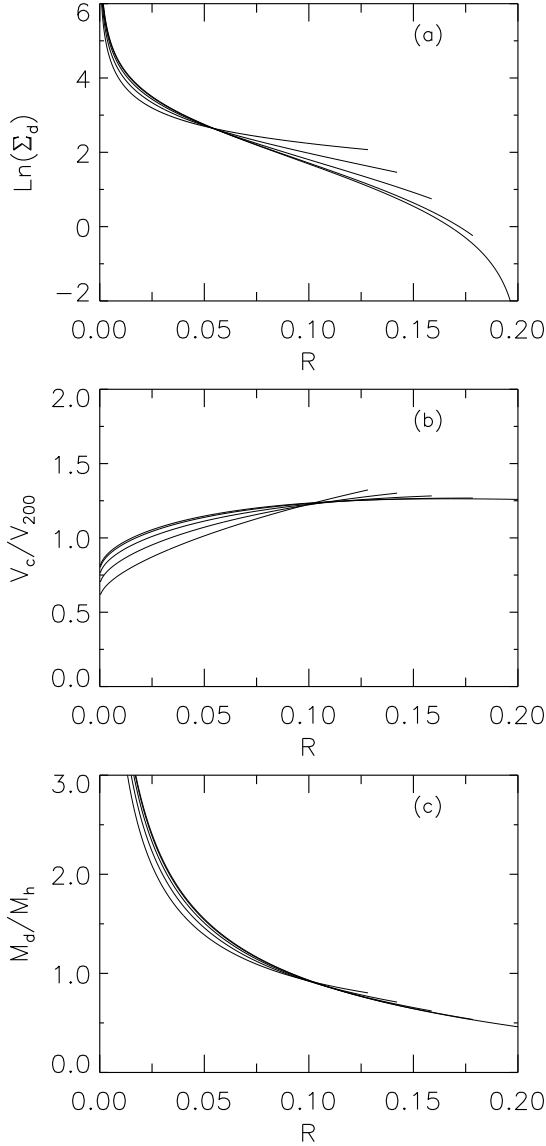


Figure 6. The model corresponding to point D in Figure 1. (a) the surface density, (b) circular velocity and (c) disk-to-halo mass ratio with $\lambda = 0.06$ and $F = 0.1$. The virialized halo is non-singular isothermal halo with constant density core size $c = 4$. The angular momentum distribution function is $f(b, \ell) = (1+b)\ell - b\ell^2$. The different curves correspond to $b = 0, 1/4, 1/2, 3/4, 1$. The disk-to-halo mass ratio increases significantly when approaching the centre.

mentum. This indicates that viscous evolution can help the creation of an apparent disk-halo ‘conspiracy’.

As can be seen from equations (21) - (26), for given c_0 (the compactness parameter defined in equation (20)), or F/λ ratio, within a given model of $f(\ell, b)$ and virialized dark halo profile $g(R)$, the normalized properties of the disks formed for $b = 0$ are very similar. In particular the disk surface density profile, rotation curve and disk-to-halo mass ratio profile scale similarly with ℓ . For example, in the case of the singular isothermal sphere (model F), equations (34)

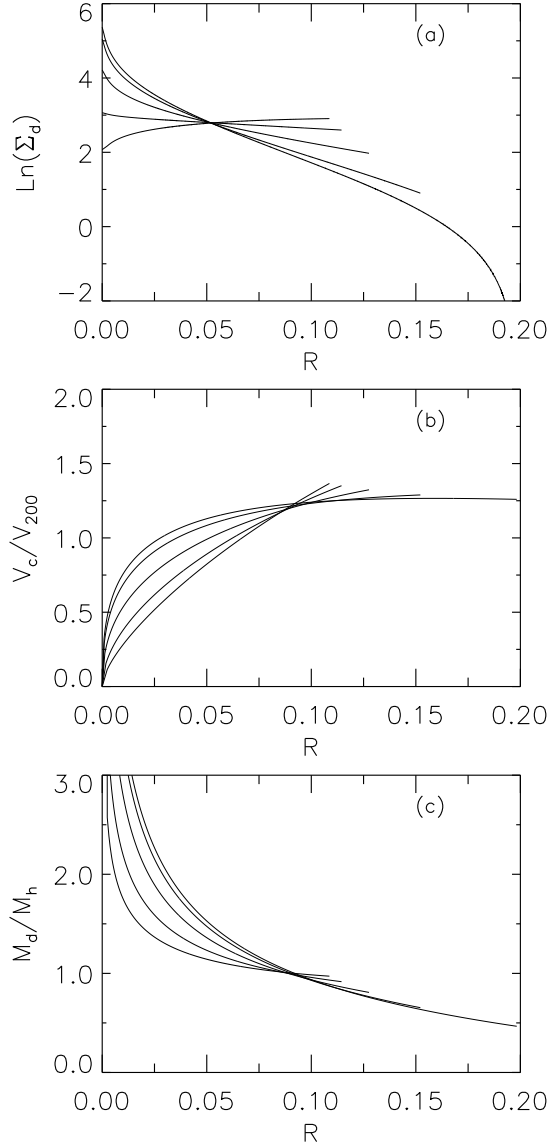


Figure 7. The model corresponding to point C in Figure 1. (a) the surface density, (b) circular velocity and (c) disk-to-halo mass ratio with $\lambda = 0.06$ and $F = 0.1$. The virialized halo is non-singular isothermal halo with core size $c = 4$. The angular momentum distribution function is $f(b, \ell) = (1 + 10b)\ell^{4/3} - 10b\ell^{22/15}$. The different curves correspond to $b = 0, 0.1, 0.3, 0.6, 1$. The disk-to-halo mass ratio increases significantly when approaching the centre.

- (37) show that for $b = 0$ the normalized disks are identical for given F/λ ratio. Thus F/λ must be an important factor in distinguishing one disk from another. The overall normalization of the surface density is $\propto F/\lambda^2$, so that again F/λ and λ enter separately and are both important.

Note that here we are not insisting that the surface density profile of the gas disk so formed be exponential, unlike previous work (Mo, Mao & White 1998). We shall however appeal to viscous evolution tied to star formation to provide a stellar exponential disk. We now turn to this.

3 THE VISCOUS EVOLUTION AND STAR FORMATION

In this paper we aim to link viscous evolution within disks and the Hubble sequence of disk galaxies. One of the motivations for invoking viscous disks is that if the timescale of angular momentum transport via viscosity is similar to that of star formation, a stellar exponential disk is naturally produced independent of the initial gaseous disk surface density profile (Silk & Norman 1981; Lin & Pringle 1987; Saio & Yoshii 1990; Firmani, Hernandez & Gallagher 1996). Angular momentum transport and associated radial gas flows (both inwards and outwards) can also, as shown above, provide a tight ‘conspiracy’ between disk and halo rotation curves, and, as demonstrated below, provide a higher phase space density in bulges as compared to disks.

The star formation rate per unit area in a disk can be represented by a modified Schmidt law involving the dynamical time and the gas density (Wyse 1986; Wyse & Silk 1989). We shall use the form of the global star formation rate per unit area, Σ_ψ , of Kennicutt (1998), based on his observations of the inner regions of nearby large disk galaxies:

$$\Sigma_\psi = \alpha \Sigma_{gas} \Omega_{gas}, \quad (40)$$

where Σ_{gas} is total gas surface density, Ω_{gas} is the dynamical time at the edge of the gas disk, and the normalization constant, related to the efficiency of star formation, has the value $\alpha = 0.017$ (Kennicutt 1998). Note that observations of the star-formation rates in the outer regions of disk galaxies suggest that it is actually *volume* density that should enter the Schmidt law, rather than surface density, and since many (if not all) gas disks flare in their outer regions, equation (40) will over estimate the star formation rate (Ferguson *et al.* 1998). This is beyond the scope of the present model, but should be borne in mind and will be incorporated in our future work.

For our models here, the edge of the initial gas disk is where $\ell = 1$, $R = R_c$ and thus $\Omega_{gas} = \Omega_c$. For halo formation redshift z_f , we can obtain the relationship between global star formation timescale and the galaxy initial conditions in the general form using equation (1), (25) and (39):

$$\begin{aligned} t_*^{-1} &= \alpha \Omega_c = \alpha V_c(r_c)/r_c \\ &= 10\alpha H(z_f) \xi (1-F)^2 (\xi m_{hc} + c_0)^2, \end{aligned} \quad (41)$$

where again m_{hc} is the solution of $1 = \xi^2 m_{hc} g^{-1}(m_{hc})$, and is the fraction of the dark halo mass that is contained within the cut-off radius of the disk. The parameters ξ and c_0 are defined in equations (13) and (20); F is the baryonic mass fraction in the initial density perturbation.

In the case of the singular isothermal halo, this relation has a simple form:

$$t_*^{-1} = 10\alpha H(z_f) \xi (1-F)^2 (1+c_0)^2. \quad (42)$$

The gas consumption timescale will be longer than the characteristic star formation timescale due to the gas returned by stars during their evolution and death. For a standard stellar Initial Mass Function, $t_g \sim 2.5t_*$ (e.g. Kennicutt *et al.* 1994).

This modified Schmidt law is based on observations of the inner regions of nearby large disk galaxies, and simple theoretical principles. Assuming it holds at all epochs allows one to estimate the properties of present-day disks from the initial conditions of earlier sections in this paper. Let us assume that the dark halo is fully virialized at redshift z_f . In keeping with the spirit of hierarchical clustering, let us allow for some star formation that could have taken place in the disk, from an earlier redshift z_i , and that the total mass of the system could increase until z_f (although to maintain the thin disk, this accretion and merging must be only of low mass, low density systems). So for any time t or redshift z between z_i and z_f ,

$$\frac{dM_g}{dt} = F \frac{dM_{tot}}{dt} - \frac{dM_*}{dt}, \quad (43)$$

$$\frac{dM_*}{dt} = \frac{M_g}{t_g(z)}, \quad (44)$$

where M_{tot} is defined in equation (1) and M_* is mass locked up into stars. In an Einstein-de-Sitter Universe, $H(z) = H_0(1+z)^{3/2}$ and $H(z)t = 2/3$. We have

$$\frac{dM_g}{dt} = A - \frac{BM_g}{t}, \quad (45)$$

where $A = \frac{3FV_{200}^3}{20G}$ and $B = \frac{8}{3}\alpha\xi(1-F)^2(1+c_0)^2$, and ξ and c_0 are expressed in terms of c_f , λ and F through equations (13) and (20) in section 2.1. Hence, from equation (1), $M_{tot} \propto \frac{A}{FH(z)}$.

Identifying the dark halo to have fixed V_{200} , independent of redshift, leads to A also being a constant, and thus the total mass grows as $M_{tot} \propto t$. This differs from the standard solution of infall onto a point, $M_{tot} \propto t^{2/3}$ (Gunn & Gott 1972).

The solution to the above equation is then

$$M_g = \frac{A}{1+B} t \left[1 + B \left(\frac{t}{t_i} \right)^{-(1+B)} \right], \quad (46)$$

where t_i corresponds to the redshift z_i of the onset of star formation. Thus at the halo formation redshift z_f , the disk gas fraction is

$$f_g(z_f) = \frac{1 + B \left(\frac{1+z_f}{1+z_i} \right)^{3(1+B)/2}}{1+B}, \quad (47)$$

Since B depends on c_f , λ and F , i.e. $B \propto \frac{c_f}{\lambda} (1-F + \frac{c_f F}{\sqrt{2}\lambda})^2$, the value of the constant B may be evaluated for $\lambda = 0.06$ and various reasonable values of F and c_f as: for $F = 0.1$, $c_f = 1/3$, $B = 0.30$; for $F = 0.05$, $c_f = 1/3$, $B = 0.23$; for $F = 0.1$, $c_f = 0.5$, $B = 0.59$; and for $F = 0.05$, $c_f = 0.5$, $B = 0.41$. For fixed λ and F , small values of B correspond to small values of c_f , and hence flatter specific angular momentum distributions.

Thus for $1+z_f \lesssim 2(1+z_i)$, $f_g(z_f) \approx 1/(1+B)$, typically $\gtrsim 2/3$.

We assume that after z_f , there is no further infall, and that the gas in the disk will be consumed with characteristic timescale $t_g(z_f)$. Thus the gas fraction of a typical disk galaxy at the present time is

$$f_g = f_g(z_f) \exp[-\delta t(z_f)/t_g(z_f)], \quad (48)$$

where $\delta t(z_f)$ is the time interval between the halo formation redshift z_f and present time $z = 0$.

Assuming an Einstein-de-Sitter universe, we have $\delta t(z_f) = t_0(1 - H_0/H(z_f))$ and $t_0H_0 = 2/3$. Thus a typical value for the present gas fraction of disk galaxies is:

$$\ln\left(\frac{f_g(z_f)}{f_g}\right) = B[(1+z_f)^{3/2} - 1]. \quad (49)$$

With the approximation $f_g(z_f) = 1/(1+B)$, we have

$$(1+z_f)^{3/2} = 1 + \frac{-\ln f_g - \ln(1+B)}{B}. \quad (50)$$

For the Milky Way Galaxy, if we adopt $5 \times 10^9 M_\odot$ for the atomic HI gas, and $1.3 \times 10^9 M_\odot$ for the molecular H_2 gas (Blitz 1996; Dame 1993), then with an estimate of $4 - 6 \times 10^{10} M_\odot$ for the total baryonic mass of the Milky Way depending on stellar exponential scale length (Dehnen & Binney 1998), we obtain gas fraction, the total gas mass includes 24% helium mass, $f_g \sim 15\%$ or even higher depending on the mass model of the Galaxy. As mentioned earlier, for fixed λ and F , small values of B correspond to small values of c_f , and hence flatter specific angular momentum distributions. For small values of the parameter B , say $B \sim 0.3$, we obtain $z_f \sim 2.4$, while for large values of B , $B \sim 0.6$, we obtain $z_f \sim 1.2$. The larger value of z_f is preferred, given what we know of the age distribution of stars in the local thin disk (e.g. Edvardsson *et al.* 1993). The effect of viscous evolution is equivalent to choosing small c_f , i.e. small values of B . So the inclusion of viscous evolution can give relatively higher halo formation redshift, which is consistent with the results from the constraint on the redshift of formation that we obtained from considerations of the size of the disk.

It should be noted that for fixed halo ‘formation’ redshift z_f , the star formation timescale $t_*^{-1} \sim \frac{1}{\lambda}(1 - F + \frac{1}{2\sqrt{2}}\frac{F}{\lambda})^2$. Again, both λ and F/λ are important. As we discussed in the previous section, the structure of the normalized disk depends strongly on F/λ while the overall normalization depends strongly on λ for fixed F/λ . As we show later, the bulge-to-disk ratio also depends on the importance of λ and F/λ . Thus many aspects of the Hubble sequence of disk galaxies – star formation timescale, disk gas fraction, bulge-to-disk ratio – depend on both λ and F/λ .

The star formation timescale derived above is independent of V_{200} , which at first sight is surprising, given that the Hubble sequence of disk galaxies has been interpreted as a sequence of star formation timescales, relative to collapse times (Sandage 1986), and observations show that the Hubble type of a disk galaxies is broadly correlated with the disk luminosity (Lake & Carlberg 1988; de Jong 1995). However, V_{200} is not an easily-observed quantity.

The present-day luminosity of a disk in our model can be written as

$$L = \frac{FM_{tot}(1-f_g)}{\gamma_*} = \frac{F[1-f_g(B, z_f)]V_{200}^3}{10GH(z_f)\gamma_*}, \quad (51)$$

with γ_* the current value of the mass-to-light ratio. Estimation of the predicted Tully-Fisher relation depends on what model parameter we use for the width of the HI line. Ob-

viously if we identify this with V_{200} we have a reasonable relationship provided that the coefficient γ_{TF} is constant, i.e. $F[1-f_g(B, z_f)]/H(z_f) = \gamma_{TF}$. This then requires that there should be a correlation between F and z_f , in the sense that for large F , z_f is large. Then we can see from equation (42) that this leads to the star formation timescale being small, implying more efficient viscous evolution, and leading to larger B/T ratio. Large z_f may be correlated with small V_{200} in the context of hierarchical-clustering cosmologies, and in that case, a short star formation time and large B/T ratio should be correlated with low luminosity, which is not consistent with observation. However, an interpretation that is compatible with observations is that high n-sigma fluctuations for fixed V_{200} can form high luminosity disks with large B/T ratio.

The Tully-Fisher relationship is not a simple relation between luminosity and V_{200} , but depends on where the circular velocity $V_c(R)$ is measured (Courteau 1997). The relationship between V_{200} and $V_c(R)$ obviously depends on the details of the halo density profile and the angular momentum distribution. From the rotation curves in fig. 3 to fig. 7, we can see that it is appropriate to choose for our estimate of V_c the circular velocity at the cutoff radius of disk, adopted as 3 three scale lengths. From equation (35), we have $V_c = V_{200}(1-F)(1+c_0)$, where $c_0 = c_f F/\sqrt{2}\lambda(1-F)$, as defined in equation (20), is the compactness of disk. Now the predicted Tully-Fisher relation is

$$L = \frac{F[1-f_g(B, z_f)]V_c^3}{10GH(z_f)\gamma_*(1+c_0)^3(1-F)^3}. \quad (52)$$

Requiring that the coefficient γ_{TF} in the Tully-Fisher relation be constant, i.e. $\gamma_{TF} \equiv F[1-f_g(B, z_f)]/H(z_f)(1+c_0)^3(1-F)^3$, then gives, from equation (42), $t_*^{-1} \propto c_0/(1+c_0)$. So for small c_0 , the star formation timescale is large, which can cause less efficient viscous evolution. So less efficient viscous evolution and small F/λ will lead to small B/T ratio. Also small c_0 is correlated with large z_f from the constancy of the coefficient in the Tully-Fisher relation. Similarly large z_f may be correlated with small V_{200} in the context of hierarchical clustering cosmology. So small c_0 and small V_{200} will lead to small V_c and lower disk luminosity. Thus this version of the predicted Tully-Fisher relation appears fully compatible with the observations. However, one should bear in mind that we have adopted a fixed constant of proportionality α in the star formation law, and this may well vary with global potential well depth (White & Frenk 1991) or local potential well depth (Silk & Wyse 1993).

A further test of the model is the relation between disk scale and circular velocity, and its variation with redshift; observations indicate that R_d/V_c is smaller at high redshift, $z \sim 1$ (Vogt *et al.* 1996; Simard *et al.* 1999). In our model there is little change in total mass between redshifts of unity and the present, and so this evolution of disk size cannot be due to the halo mass growth, as had been proposed by Mao, Mo & White (1998). Instead in our model this is due to the different and changing scale lengths of gas and stars. In our model, due to early star formation, the gas fraction at z_f is about $f_g(z_f) \sim 1/(1+B)$, typically $2/3$. It is natural that the gas component of the disk will have a larger scale length

than the stellar component. The scale length of the gas component can increase with time due to viscous evolution while the scale length of stellar component can also increase with time due to the non-linear local star formation law (Saio & Yoshi 1990). So the stellar scale length at high redshift, when the gas fraction is large, should be much smaller than the stellar scale length at present time, when gas fraction is lower. The study of detailed evolution of gas and stellar component is beyond the scope of this paper; but the prediction of stellar size evolution of our model is qualitatively consistent with the observations.

The measured distribution of R_d/V_c for the local disk galaxy sample is approximately peaked at $R_d/V_c \sim -1.5$ (R_d in kpc, V_c in kms^{-1}) with a spread from -2 to -1 (Mao, Mo & White 1998; Courteau 1996). Our estimation of the disk size or scale length in Section 2 is valid for galaxies at the present time, when the gas fraction is small. Then assuming the disk cut off radius is three scale lengths, from equation (41), $R_d/V_c = R_c/3V_c = \alpha t_*/3$, and the present R_d/V_c is an indication of the galactic global star formation timescale; further, from the constancy of γ_{TF} , the coefficient of the Tully-Fisher relation in equation (52), we have

$$R_d/V_c = \alpha t_*/3 = \frac{G}{3} \gamma_{TF} \gamma_* \frac{1 + c_0}{c_0(1 - f_g)}. \quad (53)$$

Thus this ratio is also an indication of the disk compactness. Adopting the B-band mass-to-light ratio of our local disk $\gamma_* \sim 2.5M_\odot/L_\odot$, and using the luminosity of our galaxy $L_B \sim 3 \times 10^{10}L_\odot$ and $V_c \sim 220 \text{ km s}^{-1}$ to estimate $\gamma_{TF} = L_B/V_c^3$, we can obtain that $\log(R_d/V_c) \simeq -2.0 + \log(\frac{1+c_0}{c_0(1-f_g)})$. Obviously $\log(R_d/V_c) \sim -2$ roughly corresponds to the predicted lower limit of the local sample, which is consistent with observations. The distribution of F from 0.05 to 0.2 and the distribution of λ from 0.03 to 0.12 will cause the value of the compactness parameter c_0 to spread from 0.1 to 2 approximately. Adopting typical values $F = 0.1$, $\lambda = 0.06$, $c_f = 1/3$, the peak will be located at $\log(R_d/V_c) = -1.5$ with $c_0 = 0.44$, which is again consistent with observations. The spread of R_d/V_c is simply caused by the spread in the value of compactness parameter c_0 .

4 THE FORMATION OF BULGES AND THE HUBBLE SEQUENCE

Galaxies classification schemes based on morphology are the basic first step in understanding how galaxies form and evolve (van den Bergh 1998). The bulge-to-disk luminosity ratio is one of the three basic classification criterion for the Hubble sequence (Sandage 1961). However, the relation between bulge-to-disk ratio and Hubble type has a fair amount of scatter, some of which must be related to the difficulty of a decomposition of the light profile into bulge and disk, and the bulge-to-disk ratio is dependent on the band-pass used to define the luminosity (de Jong 1996). The current observational data show that bulges can be diverse and heterogeneous (Wyse, Gilmore & Franx 1997). Some share properties of disks and some are more similar to ellipticals. Models of bulge formation can be classified into several categories: the

bulge is formed from early collapse of low angular momentum gas, with short cooling time and efficient star formation (Eggen *et al.* 1962; Larson 1976 – who invoked viscosity to transport angular momentum away from the proto-bulge; van den Bosch 1998); the bulge is formed from merging of disk galaxies (Toomre & Toomre 1972; Kauffmann, White & Guiderdoni 1993); the bulge is formed from the disk by secular evolution process after bar instability (Combes *et al.* 1990; Norman, Sellwood & Hasan 1996; Sellwood & Moore 1999; Avila-Reese & Firmani 1999); the bulge is formed from early dynamical evolution of massive clumps formed in disk (Noguchi 1999). However it is speculated that large bulges, which tend to have de Vaucouleur’s law surface brightness profiles, share formation mechanisms with ellipticals, while smaller bulges, which tend to be better fit by an exponential profile, are formed from their disks through bar dissolution. It should be noted that the significantly higher phase space density of bulges when compared to disks suggests that gaseous inflow should play a part in the instability (Wyse 1998), just as invoked in earlier sections of this paper, for other reasons.

Here we only consider this latter case, the formation of small bulges from the disk. Early studies of disk instabilities showed that Toomre’s local stability criterion $Q > 1$ is also sufficient for global stability to axisymmetric modes (Hohl 1971; Binney & Tremaine 1987). It is known that the bar instability requires a similar condition (Hockney & Hohl 1969; Ostriker & Peebles 1973). Efstathiou, Lake & Negroponte (1982) used N-body techniques to study the global bar instability of a pure exponential disk embedded in a dark halo and proposed a simple instability criterion for the stellar disk, based on the disk-to-halo mass ratio. However, it has been argued recently that there is no such simple criterion for bar instability (Christodoulou, Shlosman & Tohline 1995; Sellwood & Moore 1999). Further, recent N-body simulations (Sellwood & Moore 1999; Norman, Sellwood & Hasan 1996) show that every massive disk form a bar during the early stages of evolution, but later the bar is destroyed by the formation of a dense central object, once the mass of that central concentration reaches several percent of the total disk mass. This can be understood in terms of the linear mode analysis work and nonlinear processes of swing amplifier and feed back loops (Goldreich & Lynden-Bell 1965; Julian & Toomre 1966). Toomre (1981) argued that the bar-instability can be inhibited in two ways: one is that a large dark halo mass fraction can reduce the gain of the swing amplifier, while the other is that feedback through the centre can be shut off by a inner Lindblad resonance (ILR). The dense central object can destroy the bar via the second of these mechanisms. However, most of these studies assume that the dark halo has a constant density core. On the contrary, we have shown that dark halo profile cannot have a constant density core after adiabatic infall, if one starts from physical initial conditions. It will be interesting to study bar formation under different disk-halo profiles in addition to the well-studied harmonic core.

We will for simplicity adopt the simple criterion of Efstathiou, Lake & Negroponte (1982), interpreted to deter-

mine the size of a bar-unstable region, with the radial extent of the bar, r_b defined by

$$M_d(r_b)/M_h(r_b) \geq \beta, \quad (54)$$

with the value of the parameter β chosen to fit observations. As we have argued in section 2, F/λ is the important quantity determining the overall normalization of the disk surface density. From N-body simulations (Warren *et al.* 1992; Barnes & Efstathiou 1987; Cole & Lacey 1996; Steinmetz & Bartelmann 1995), the distribution of λ can be fit by a log-normal distribution:

$$P(\lambda)d\lambda = \frac{1}{\sqrt{2\pi}\sigma_\lambda} \exp\left[-\frac{\ln^2(\lambda/\lambda_0)}{2\sigma_\lambda^2}\right] \frac{d\lambda}{\lambda}, \quad (55)$$

where $\lambda_0 = 0.06$ and $\sigma_\lambda = 0.5$ (this result is fairly independent of the slope of the power spectrum of density fluctuations).

What of the possible range of the baryonic fraction F ? Some previous studies suggested that $F \sim \lambda$ as an explanation of the disk-halo ‘conspiracy’ (Fall & Efstathiou 1980; Jones & Wyse 1983; Ryden & Gunn 1987; Hernandez & Gilmore 1998). Some interpretations of the observed Tully-Fisher relationship suggest that indeed F is not invariant (McGaugh & de Blok 1998). Here we shall assume that the distribution of F , similar to λ , is log-normal, centred at $F_0 = 0.1$ with $\sigma_F = 0.05$. So F is mainly within the range $0.05 \sim 0.2$.

We generated a Monte Carlo sample of disks, with fixed halo V_{200} and halo formation redshift z_f , but with values of F and λ following the above distributions. Then for given virialized dark halo profiles $g(R)$ and angular momentum distribution $f(b, \ell)$ in Figure 1, we can calculate the star formation timescale from equation (41). The parameter b represents the efficiency of viscous evolution; on the assumption that the viscous timescale is equal to the star formation timescale, we can use a simple linear correlation between the value of b and the star formation timescale. Then the value of parameter b can be obtained. From equations (21), (22), (23), (26), (50) and (54), one can calculate the bulge-to-disk ratio and final disk gas fraction.

Thus we can plot B/T ratio versus disk gas fraction, for the whole Monte Carlo sample, confining the parameter space of λ and F to give small bulges with $B/T < 0.5$. Larger values of B/T would correspond to such an unstable disk that the exercise is invalid. Disks that are too stable, having low F/λ or large λ , will evolve little and probably end up as low surface brightness systems.

Figure 8a shows model F, representing the singular isothermal halo. Assuming the typical values $\lambda = 0.06$ and $F = 0.1$, then the choice of $\beta \sim 0.8$ is required to allow the existence of bulges. This is just the value of β used in the global bar instability criterion (Efstathiou, Lake & N-groponte 1982). For this model the disk-to-halo mass ratio varies little with radius (as shown in Figure 3a), so the B/T ratio is strongly dependent on λ/F . Only a small range of values of λ/F is allowed, so as to not over-produce either bulge-less disks or completely unstable disks.

The relation between B/T ratio and gas fraction for this model is given in Figure 8b; there a general trend in

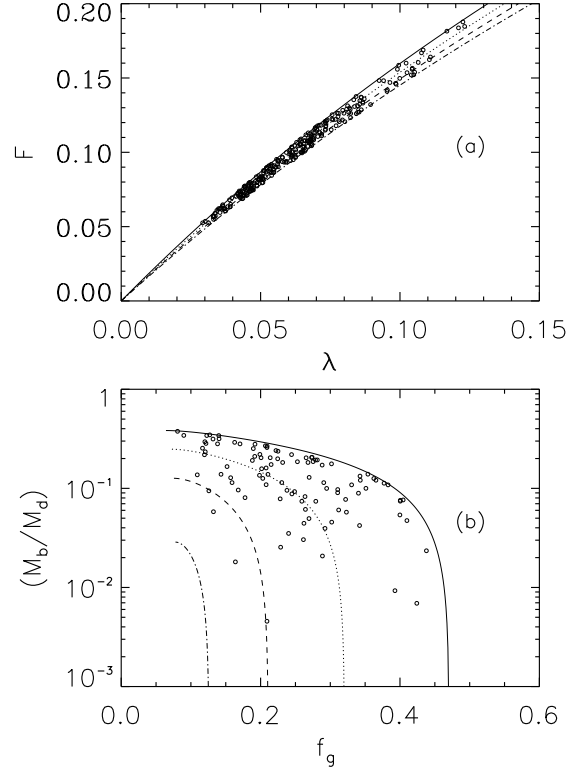


Figure 8. The model corresponding to point F in Figure 1. (a) The sample of disk galaxies with different λ and F . (b) The relation between B/T ratio and gas fraction for these sample galaxies at current age. The different curves in this plot correspond to different values of $(1 - F)\lambda/F \approx \lambda/F$, which sets the overall trend.

the observed sense, with large scatter. The different curves in this plot correspond to different values of λ/F , which sets the overall trend.

Figure 9 (a,b) shows the equivalent plots of model E, representing a Hernquist profile halo model, which is probably a more realistic case. Here the the disk-to-halo mass ratio varies strongly with radius when approaching the centre, and the allowed parameter space for values of λ and of F that allowing the formation of bulges can be large. Overly-unstable disks are denoted by asterisk symbols in Figure 9a, and low surface-brightness disks are denoted by cross symbols. The relation between B/T ratio and gas fraction is similar to that for the isothermal halo.

4.1 Constraints from the Milky Way

The Milky Way bulge is reasonably well-fit by an exponential profile, with a scale-length approximately one-tenth that of the disk (Kent *et al.* 1991). The morphology of the bulge is consistent with some triaxiality (Blitz & Spergel 1991; Binney *et al.* 1997). Perhaps the Milky Way is a system in which the bulge has formed from the disk, through a bar instability? Observations show no evidence for a significant young or even intermediate-age stellar population in the field population of the Galactic Bulge (Feltzing & Gilmore 1999),

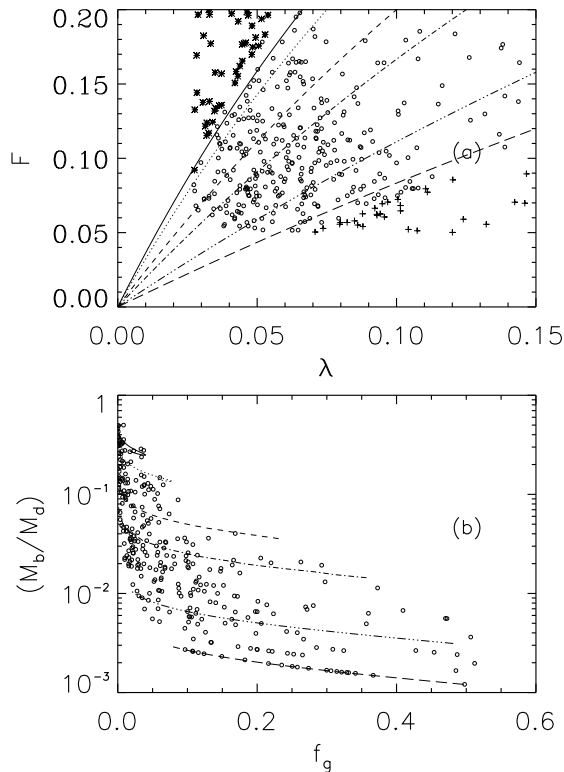


Figure 9. The model corresponding to point E in Figure 1. (a) The sample of disk galaxies with different λ and F . Overly-unstable disks are denoted by asterisk symbols. Bulgeless disks or low surface-brightness disks are denoted by cross symbols. (b) The relation between B/T ratio and gas fraction for these sample galaxies at current age. The different curves in this plot correspond to different values of $(1 - F)\lambda/F \approx \lambda/F$, which sets the overall trend.

despite their being ongoing star formation in the inner disk. This implies that if the bulge were formed from the disk through bar dissolution, only one such episode is allowed, and this should have happened at high redshift. In the context of the present model, the lower star formation rates and longer viscosity timescales of later times act to stabilize the system. However, it remains to be seen if the observed relative frequencies of bars, bulges and central mass concentration is consistent with the models of bar dissolution.

5 SUMMARY

In the context of hierarchical clustering cosmology, the dark halo of a disk galaxy can be formed by quiescently merging small sub-halos into the primary dark halo, or by smoothly accreting matter into the dark halo. We derive the generic solution to the adiabatic infall model of disk galaxy formation pioneered by many authors (Mestel 1963; Fall & Efstathiou 1980; Gunn 1982; Faber 1982; Jones & Wyse 1983; Ryden & Gunn 1987; Dalcanton, Summer & Spergel 1997; Mo, Mao & White 1998; Hernandez & Gilmore 1998). Through exploring the allowed parameter space of dark halo

profile and angular momentum distribution function, we show that the central halo density profile should be cuspy, with the power law index ranging from -0.75 to -2 , in the central regions where the disk mass dominates.

Using a modified Schmidt law of global star formation rate, we derive a simple scaling relationship between the disk gas fraction and the assembly redshift. We explicitly allow a distribution in the values of the baryonic mass fraction, F , in addition of the distribution in values of the spin parameter λ . These two are found to play different role in determining the structural properties of the final disk, the star formation properties and bulge-to-disk ratio.

We mimic viscous evolution of disks by varying the specific angular momentum distribution of the disk, to redistribute angular momentum as a function of time. We derive a consistent picture of the formation of galaxies like the Milky Way, with old stars in the disk. Under the assumption that the viscous evolution timescale is equal to the star formation timescale, we can further combine the λ and F with the efficiency of angular momentum redistribution caused by viscosity. Assuming that small bulges are formed from their disks through bar dissolution, we can use the global bar instability condition to obtain bulge-to-total ratio, and explore the dependence on F , λ and the viscous evolution efficiency.

The inclusion of viscous evolution has the merits of addressing several important issues: the conspiracy between disk and halo, the formation of the exponential profile of stellar disk, the high phase space density of bulges. We have presented an analytic treatment, to illustrate these points and identify areas of particular need for more work.

ACKNOWLEDGMENTS

We acknowledge support from NASA, ATP Grant NAG5-3928. BZ thanks Colin Norman, Jay Gallagher for helpful comments. RFGW thanks all at the Center for Particle Astrophysics, UC Berkeley, for their hospitality during the early stages of this work.

REFERENCES

- Avila-Reese, V. & Firmani, C., 1999, in Carral, P. & Cepa, J., eds, ASP Conf. Ser. Vol. 163; Star Formation in Early-Type Galaxies. Astron Soc. Pac., San Francisco, p.243.
- Barnes, J. & Efstathiou, G., 1987, ApJ, 319, 575.
- Binney J., Gerhard, O. & Spergel, D., 1997, MNRAS, 288, 365.
- Binney J. & Tremain, S., 1987, Galactic Dynamics, Princeton University Press
- Blitz, L., 1996, in Latter, W.B., Radford, S.J.E., Jewell, P.R., Mangum, J.G. & Bally, J., eds, Proc IAU Symp. vol. 170, CO: Twenty-Five Years of Millimeter-Wave Spectroscopy. Kluwer Academic Publishers, p11.
- Blitz, L. & Spergel, D., 1991, ApJ, 370, 205.
- Blumenthal, G.R., Faber, S.M., Flores, R. & Primack, J.R., 1986, ApJ, 301, 27.
- Casertano, S. & van Gorkom, J.H., 1991, ApJ, 101, 1231.
- Christodoulou, D.M., Shlosman, I. & Tohline, J.E., 1995, ApJ, 443, 563.

- Cole, S. & Lacey, C., 1996, MNRAS, 281, 716.
- Combes, F., Debbasch, F., Friedli, D., & Pfenninger, D., 1990, A&A, 233, 82.
- Courteau, S., 1996, ApJS, 103, 363.
- Courteau, S., 1997, AJ, 114, 2402.
- Dalcanton, J.J., Spergel, D.N., & Summers, F.J., 1997, ApJ, 482, 659.
- Dame, T., 1993, in "Back to the Galaxy", eds. Holt, S.S & Verter, F., AIP Press: New York, p267.
- de Jong, R.S., 1995, Ph.D. Thesis, University of Groningen.
- de Jong, R.S., 1996, A&A, 313, 45.
- Dehnen, W. & Binney, J., 1998, MNRAS, 294, 429.
- Edvardsson, B., Andersen, J., Gustafsson, B., Lambert, D.L., Nissen, P.E. & Tomkin, J., 1993, A&A, 275, 101.
- Efstathiou, G., Lake, G. & Negroponte, J., 1982, MNRAS, 199, 1069.
- EGgen, O., Lynden-Bell, D. & Sandage, A., 1962, ApJ, 136, 748.
- Faber, S.M., 1982, in Bruck, H.A., Coyne, G.V. & Longair, M.S., eds, Astrophysical Cosmology, Pontificia Academia Scientiarum, p191.
- Fall, S.M. & Efstathiou, G., 1980, MNRAS, 193, 189.
- Feltzing, S. & Gilmore, G., 1999, in Spite, M., eds, Galaxy Evolution: Connecting the Distant Universe with the Local Fossil Record, Kluwer Academic Publishers, p71.
- Ferguson, A.M.N., Wyse, R.F.G., Gallagher, J. & Hunter, D.A., 1998, ApJ, 506, L19.
- Firmani, C., Hernandez, X. & Gallagher, J., 1996, A&A, 308, 403.
- Goldreich, P. & Lynden-Bell, D., 1965, MNRAS, 130, 125.
- Gunn, J.E., 1982, in Bruck, H.A., Coyne, G.V. & Longair, M.S., eds, Astrophysical Cosmology, Pontificia Academia Scientiarum, p233.
- Gunn J.E. & Gott R., 1972, ApJ, 176,1.
- Hernandez, X. & Gilmore, G., 1998, MNRAS, 294, 595.
- Hernquist, L., 1990, ApJ, 356, 359.
- Hockney, R.W. & Hohl, F., 1969, AJ, 74, 1102.
- Hohl, F., 1971, AJ, 76, 202.
- Jones, B.J.T. & Wyse, R.F.G., 1983, A&A, 120, 165.
- Julian, W.H. & Toomre, A., 1966, ApJ, 146, 810.
- Kauffmann, G., White, S.D.M. & Guiderdoni, B., 1993, MNRAS, 264, 201.
- Kennicutt, R.C., 1998, ApJ, 498, 541.
- Kennicutt, R.C., Tamblyn, P. & Congdon, C.W., 1994, ApJ, 435, 22.
- Kent, S.M., Dame, T.M. & Fazio, G., 1991, ApJ, 378, 131.
- Lake, G. & Carlberg, R.G., 1988, AJ, 96, 1587.
- Larson, R.B., 1976, MNRAS, 176, 31.
- Lin, D.N.C. & Pringle, J.E., 1987, ApJ, 168, 603.
- McGaugh, S.S. & de Blok, E., 1998, in "Galactic Halos", eds. Zaritsky, D., APS Conference Series vol. 136, p210.
- Mestel, L., 1963, MNRAS, 126, 553.
- Mao, S., Mo, H.J., & White, S.D.M., 1998, MNRAS, 297, L71.
- Mo, H.J., Mao, S. & White, S.D.M., 1998, MNRAS, 295, 319.
- Navarro, J.F., Frenk, C.S. & White, S.D.M., 1997, ApJ, 490, 493.
- Navarro, J.F. & Steinmetz, M., 1997, ApJ, 478, 13.
- Noguchi, M., 1999, ApJ, 514, 27.
- Norman, C.A., Sellwood, J. & Hasan, H., 1996, ApJ, 462, 114.
- Ostriker, J.P. & Peebles, P.J.E., 1973, ApJ, 186, 487.
- Ostriker, J.P., 1990, in "Evolution of the Universe of Galaxies", ASP Conference Proceedings Vol. 10, eds. Kron, R.G., p25.
- Peebles, P.J.E., 1993, Principle of Physical Cosmology, Chap. 22.
- Quinn, T. & Binney, J., 1992, MNRAS, 255, 729.
- Ryden, B.S. & Gunn, J.E., 1987, ApJ, 318, 15.
- Saio, H. & Yoshii, Y., 1990, ApJ, 363, 40.
- Sandage, A., 1961, The Atlas of Galaxies (Washington, D.C., Carnegie Institution of Washington)
- Sandage, A., 1986, A&A, 161, 89.
- Sellwood, J.A. & Moore, E.M., 1999, ApJ, 510, 125.
- Silk, J. & Norman, C.A., 1981, ApJ, 247, 59.
- Silk, J. & Wyse, R.F.G., 1993, Phys. Rep. 231, 295.
- Simard, L., Koo, D.C., Faber, S.M., Sarajedini, V.L., Vogt, N.P., Phillips, A.C., Gebhardt, K., Illingworth, G.D. & Wu, K.L., 1999, ApJ, 519, 563.
- Steinmetz M. & Bartelmann M., 1995, MNRAS, 272, 570.
- Toomre, A., 1981, In "Structure and Evolution of Normal Galaxies", eds. Fall, S.M. & Lynden-Bell, D., Cambridge University Press, p111.
- Toomre, A. & Toomre, J., 1972, ApJ, 178, 623.
- van den Bergh, S., 1998, Galaxy Morphology and Classification, Cambridge University Press.
- van den Bosch, F.C., 1998, ApJ, 507, 601.
- van der Kruit, 1987, A&A, 173, 59.
- Vogt, N.P., Forbes, D.A., Phillips, A.C., Gronwall, C., Faber, S.M., Illingworth, G.D. & Koo, D.C., 1996, ApJ, 465, L15.
- Warren, M.S., Quinn, P.J., Salmon, J.K. & Zurek, W.H., 1992, ApJ, 399, 405.
- White, S.D.M. & Frenk, C.S., 1991, ApJ, 379, 52.
- White, S.D.M. & Rees, M.J., 1978, MNRAS, 183, 341.
- Wyse, R.F.G., 1986, ApJ, 311, L41.
- Wyse, R.F.G., 1998, MNRAS, 293, 429.
- Wyse, R.F.G., Gilmore, G. & Franx, M., 1997, ARA&A, 35, 637.
- Wyse, R.F.G. & Silk, J., 1989, ApJ, 339, 700.
- Zurek, W.H., Quinn, P.J. & Salmon, J.K., 1988, ApJ, 330, 519.